All-in-one Quantum Diamond Microscope for Sensor Characterization: Supplemental Document

Connor Roncaioli,[1,2] Connor A. Hart,[2] Ronald Walsworth,[2] and Donald P. Fahey[1,2]
[1)] *DEVCOM Army Research Laboratory*
[2)] *Quantum Technology Center, University of Maryland*

(*Electronic mail: connor.a.roncaioli.civ@army.mil)

(Dated: 30 September 2024)

This supplemental material provides additional information about the techniques and error analysis involved in the all-in-one quantum diamond microscope (QDM).

I. INSTRUMENT

Fig. S1 is a schematic diagram of each component involved in the full apparatus. Fig. S2 shows the all-in-one QDM in CAD render.

A. Optical Control

A Lighthouse Photonics Sprout DPSS laser (up to 10 Watt output power) illuminates NVs for PL measurements. Typical input power to the sample is 80 mW for confocal measurements and 1 W for wide-field imaging. An acoustic optical modulator (AOM) controls optical switching and intensity of the laser, with $\approx$100 ns switching time. The optical polarization is controlled by a half-waveplate, a spatial light filter selects the TEM_{00} mode for spatial consistency, and an automated beam magnifier controls the collimated beam spot size, resulting in a collimated zeroth Gaussian mode beam with a controllable beam width and well-defined linear polarization. A beam spot matched to the input objective is ideal for confocal measurements, while a larger beam ($\approx$5 mm) is necessary for full-sample illumination.

Epi-illumination for point measurements is achieved by directing the laser through the top objective (Olympus PLN 4$\times$) to excite a small ($\approx$10 µm) region of the NV layer in the diamond samples. Full-sample illumination for imaging uses a long-focal length cylindrical lens (f=300 mm) and a periscope that is located next to the microscope body. To evenly illuminate the entire sample, the periscope is designed to bring the beam in at a shallow (<4°) angle, while a cylindrical lens is used to focus the beam down along the axis perpendicular to the sample face.

Optical birefringence measurements of the diamond sample utilize a green LED (530 nm) with 360° rotatable linear polarization, which swaps with the top objective using a switchable mount. Light transmits through the diamond sample then passes through a circular-polarization analyzer, which sits in a filter turret along the lower imaging pathway, after the below-sample objective. If the analyzer is removed, the LED directly images the sample, which is useful for preliminary alignment and establishing focus on the intended sample surface.

B. Bias field control

Moving between different sensing modalities requires vector control of the bias magnetic field. With the bias magnetic field along the diamond <111> axis, the spin properties of a single NV orientation can be studied. With the bias magnetic field along the <100> axis, the spin transition frequencies for all four NV orientations overlap and increase contrast. When doing CW-ODMR for all NV orientations, the bias field is set to an intermediate low-symmetry direction that evenly splits the NV spin resonances for the four orientations in order to maximize the spectral dynamic range of each NV orientation class. The QDM uses a $\approx$5 mT magnetic field because a large field is advantageous to increase the spectral dynamic range available. Field strength can be adjusted by symmetrically moving the magnets closer to or further from the diamond sample.

Bias field control uses a system of SmCo magnets mounted on a dual-axis motorized gantry. The gantry provides angular control of about 60° around the azimuthal and polar angles. This range exceeds the $\approx$ 55° required along either axis in order to fully cover the fundamental symmetry group (C_{3v}) of diamond, allowing alignment of the bias magnetic field along any and all of the four NV orientations. SmCo bias magnets are used instead of Helmholtz coils to apply a strong, uniform magnetic field due to their thermal stability and independence from DC power fluctuations. Field homogeneity was <1% across mm-scale diamond samples, as measured using the CW-ODMR technique and was found to vary by <1%, confirming sufficient bias field homogeneity. If further control over the bias field is required, Helmholtz coils are a viable alternative or supplement to permanent magnets.

C. Microwave Control

A loop gap resonator (LGR) tuned to $\approx$2.87 GHz delivers a MW signal for NV manipulation, with typical Rabi frequency of a few-MHz (> NV $\frac{1}{T_2^*}$) across a mm-size diamond sample and Q $\approx$35 and hence bandwidth $\approx$80 MHz. A SRS SG386 signal generator with I/Q control option connected to a fast MW switch and a 16 W amplifier supplies a MW signal in the 2700-3000 MHz band to the LGR. Phase-dependent pulsed protocols depend on I/Q control, e.g. Ramsey and Hahn echo.

The LGR has a wide central loop about 8 mm across, which

both enhances MW signal amplitude and intensity across the cavity.[?] Use of glass as a dielectric shim increases the LGR bandwidth, allowing all NV spin resonances to be addressed, including pulsed measurements across a few-mm diamond sample. MW signals are provided to the LGR using a simple shorted loop antenna inductively coupled to the 5 mm outer loops. In future work, a split ring antenna and a stub tuner could be used to enhance MW coupling.

D. Optical Collection

There are two primary optical detection pathways, both of which use a 4× NA=0.1 objective with 5 mm focal length for a diffraction-limited resolution of 3 µm at 600 nm (Olympus PLN 4×). In the confocal path, a long-pass dichroic is used to direct the pump laser into the top objective. The top objective also collects NV PL, which passes through the dichroic and into a collection pathway. A spatial filter collects only PL from a region of uniform illumination at the center of the pump region, as well as confocally limits the z-axis collection region. If high signal intensity is preferred, the collection spatial filter can be removed to collect PL from the low-intensity region around the focal point of the objective, as well as from NVs that are out of focus. A flipper mirror then directs the collected PL either to a photodiode for time-resolved PL intensity measurements, or to a spectrometer.

Below the sample stage is a second objective for wide-field imaging, limited to a field of view of 5 mm. NV PL collected by this objective passes through a 633 nm longpass filter (Semrock LP02-633RE-25), and focuses onto a CMOS camera with a 200 mm tube lens (Basler aca1920-155um). This optical detection pathway is compatible with low-angle ($< 4^\circ$) illumination of the entire sample; or with pump light provided via the top objective, in which case the exact point of NV excitation can be determined by comparison with the PL location from a mapped image of the sample. To measure optical birefringence of the diamond sample, the dichroic is removed and a circular polarization filter is selected. In this way, polarized green LED light passed through the sample can be imaged without having to realign either the objective or the eyepiece optic, ensuring that NV PL collected from other measurements is co-aligned with the birefringence measurement.

E. Program Control and Data Analysis

Equipment timing is controlled by ultrafast digital outputs from a pulseblaster (PBESR-PRO-500-USB-RM). Analog control of devices and analog input from photodiodes is controlled by an National Instruments USB-6363 digital acquisition board (NI-DAQ). The NI-DAQ is timed to the same clock used by the pulseblaster in order to prevent timing drift between the two devices. Operation of the all-in-one QDM is performed using customized python software.

II. DATA FITTING

Imaged data sets in this work are three-dimensional data cubes. Two array axes encode spatial (X, Y) information, and a third axis is for the dependent variable of a given measurement, typically frequency (CW-ODMR) or characteristic measurement time (Ramsey, Hahn Echo etc.). Finally, the resident float for a given array element is the dependent variable. For CW-ODMR, Rabi, and T_1 relaxometry measurements, this is contrast:

$$\text{contrast} = \frac{\mathrm{I_{MWon}}}{\mathrm{I_{MWoff}}} \tag{1}$$

For phase-sensitive measurements, such as Ramsey and Hahn echo, the dependent variable is visibility:

$$\text{visibility} = \frac{\mathrm{I_{MW+}} - \mathrm{I_{MW\text{-}}}}{\mathrm{I_{MW+}} + \mathrm{I_{MW\text{-}}}} \tag{2}$$

A predictive function is fit to these variables in order to extract a parameter of interest. E.g., T_2 is calculated by identifying the characteristic decay time of the Hahn echo visibility. Such fitting is straightforward with conventional analysis packages for a single dataset (i.e., along one axis of the data cube corresponding to data from a given pixel). However fitting rapidly becomes non-trivial for mm-scale images that are on the order of 1000×1000 pixels, corresponding to $\approx 10^6$ data sets.

T_2 is determined by a fit to a simple decaying exponential:

$$\text{visibility}(\mathrm{T_2}) = \mathrm{A}e^{-\tau\times\kappa(\mathrm{T_2})} \tag{3}$$

T_1 is determined by a fit to a stretched decaying exponential:

$$\text{contrast}(\mathrm{T_1}) = 1 - \mathrm{A}e^{-\tau\times\kappa(\mathrm{T_1})^{\varepsilon}} \tag{4}$$

where $\varepsilon \approx 1$, the stretching term, is allowed to freely vary in the initial fit, but is fixed for the pixel-by-pixel GPU analysis.

Rabi frequency is determined by a fit to a decaying sinusoid with functional form

$$\text{contrast}(\text{Rabi}) = 1 - \frac{\mathrm{A}}{2}(1 - \cos(\tau \times 2\pi \mathrm{f})e^{-\tau\times\kappa(\text{Rabi})}) \tag{5}$$

with f being the Rabi frequency (in Hz).

T_2^* from Ramsey is measured with the applied MW signal detuned by $\approx$5 MHz from the NV center frequency: accordingly the relevant functional form for fitting is multiple overlapped decaying sinusoids corresponding to this detuning:

$$\begin{aligned}\text{visibility}(\text{Ramsey}) = [\mathrm{A_{-1}}(1 - \sin(\tau \times 2\pi(\mathrm{f}\text{-}\delta)) \\ + \mathrm{A_0}(1 - \sin(\tau \times 2\pi(\mathrm{f})) \\ + \mathrm{A_{+1}}(1 - \sin(\tau \times 2\pi(\mathrm{f}+\delta))]e^{-\tau\times\kappa(\text{Ramsey})}\end{aligned} \tag{6}$$

where δ is the relevant NV hyperfine splitting for 14N (isotope used in diamond sample studied in present work), and f$\approx$5 MHz is the detuning. Note that for an NV diamond sample with 15N isotopic purification, the Ramsey visibility measurement has two detuned resonances instead of three. In the above fits, A or A_i are freely varying amplitude parameters, κ are the decay constants of interest, and τ are the free precession interval for T_2 and T_2^* and the free decay interval for T_1.

CW-ODMR is slightly more complicated: first the data is averaged together into smaller frames; then a peak-fitting algorithm is used to determine the 3 hyperfine locations for each individual NV resonance class. Finally, the location of these peaks is used to seed the following fit function:

$$\begin{aligned}\text{contrast(CW-ODMR)} = 1 - \text{A}(&L(\text{f}_i\text{-}\delta,\Gamma) \\ &+L(\text{f}_i,\Gamma) + L(\text{f}_i\text{+}\delta,\Gamma))\end{aligned} \tag{7}$$

where A is once again a free amplitude parameter, δ is the hyperfine splitting, Γ is the CW-ODMR linewidth, f_i is the center frequency of the NV resonance class, and L(f,Γ) is a Lorentzian. This fitting is repeated per NV subclass for a total of eight sequential fits.

GPU enabled parallel computing resources allow data fits on the time scale of minutes. In the present work, GPUfit is employed: a Levenberg-Marquardt based non-linear least squares fitting package that utilizes Nvidia's CUDA toolset to enact computation on the GPU.[?] The Levenberg-Marquardt algorithm has strict limitations, including limited robustness that can cause convergence to incorrect parameters if the initial estimate parameters are far away from the global solution to the least squares problem. For this reason, seed parameters are found using more advanced scipy least squares methods on averaged regions of the initial dataset, corresponding to a (N$\times$N) dicing of the X-Y plane so that each seed value is a close approximate of the final solution before beginning LM fitting, with $1 \leq N \leq 10$. This approach reduces the problem to a small number of serially-calculated best fits ($\approx$ 100) using more reliable fitting methods, before moving to the GPU to process the finer details.

Uncertainty and error in NV diamond sensing comes from several sources, predominately photon shot noise from the NV PL readout and from power-variation in the laser and microwave sources.[?] For the all-in-one QDM described here, there is also a small but discernible effect from readout noise of the camera sensor. Evaluating fit uncertainty independently for each of over 1 million data sets in the present study, as well as achieving convergence of various fits to the relevant parameters, is very challenging, nonetheless, several tools exist to assess fit appropriateness for a large ensemble of similar measurements. First, semi-random inspection of several distributed data-sets is used as a proxy for the overall repeatability and accuracy of the ensemble of measurements; in particular, the aim is to choose extremal data-sets, e.g., from the edges of the sample or from the region of highest and lowest laser illumination intensity, in order to confirm convergence and consistency of measurements under many conditions. An example of a single Ramsey data set is provided in Fig. S3b, showing reasonable agreement between a fit and a single-pixel data set. Additionally, inspection is performed of example diamond sample regions of minimal strain to evaluate the convergence of fit parameters. This approach uses the observed near-random noise of the data set to approximate Gaussian noise on the input data, and provides an estimation for the variance of the fit fidelity: see Fig. S3f and Table S1 for the standard deviation values calculated for an example region. Finally, spatial plots can be made of the chi squared (χ^2) outputs of fits to data, providing insight into regions of good and poor fitting. Some degree of variance is expected between regions of high and low signal-to-noise ratio (SNR); however, if the fit function and seed parameters are well chosen, the χ^2 will stay below a characteristically low value, given the number of free parameters and the data set size. An example of this process is demonstrated in Fig. S3c, where the χ^2 map shows several interesting features. Notably, the edges of the map, where optical transmission and collection efficiency is poor, have high-χ^2 values, which is expected for lower laser illumination and NV PL intensities, corresponding to lower measurement SNR. Second, regions of fast NV dephasing (low-T_2^* value) have much lower-χ^2 values. Although this result appears counter-intuitive, strong dephasing results in visibility $\approx$0 for most of the data set, leading to accurate fitting and uniformly low-χ^2 values in these regions. Finally there is a visible grid pattern underlining the data set, which is a result of readout noise in the CMOS camera, resolved by sensitive fitting techniques.

III. MAGNETIC SENSING

CW-ODMR can be used for magnetic sensing in addition to the other listed modalities. This technique may be a particularly useful tool for diamond developers using high-pressure high-temperature (HPHT) synthesis, as ferromagnetic and paramagnetic defect inclusions are a concern in this growth method. For chemical vapor deposition (CVD) samples (as in this paper) CW-ODMR for magnetic sensing is typically less insightful, though it can help identify where strain degrades magnetic sensing capability. In Fig. S4 we detect a petal in a map of CW-ODMR detected strain, which is a well-known indicator of a line defect cluster. In the associated T_2^* we see that Ramsey field sensing is negatively degraded by the inhomogenous strain environment. By measuring the symmetric CW-ODMR lineshifts we can reconstruct B_1, the magnetic field along a given NV axis. The result is a magnetic field feature that is co-located with the non-magnetic defect bundle, indicating that this is a spurious feature in the magnetic field map.

IV. ACID CLEANING AND X-RAY SPECTROSCOPY

Samples are cleaned with a bench-top safe perchlorate etch process[?] . Perchlorate, nitric, and sulfuric acids are mixed in a 5mL:5mL:5mL ratio solution. Diamond samples are added to this solution, and then the beaker is heated to 200°C in order

TABLE S1. Standard deviation values calculated from boxed region in Fig. S3 used to estimate the noise floor of each measurement modality.

Modality	Median value	Standard deviation
CW-ODMR	$\overline{\sigma}_{\mathrm{Diag}} = 1.2\,\mathrm{MPa}$	$\sigma(\sigma_{\mathrm{Diag}}) = 0.7\,\mathrm{MPa}$
CW-ODMR	$\overline{\sigma}_{\mathrm{XY}} = 0.7\,\mathrm{MPa}$	$\sigma(\sigma_{\mathrm{XY}}) = 0.5\,\mathrm{MPa}$
CW-ODMR	$\overline{\sigma}_{\mathrm{YZ}} = 0.7\,\mathrm{MPa}$	$\sigma(\sigma_{\mathrm{YZ}}) = 0.6\,\mathrm{MPa}$
CW-ODMR	$\overline{\sigma}_{\mathrm{ZX}} = 0.7\,\mathrm{MPa}$	$\sigma(\sigma_{\mathrm{ZX}}) = 0.4\,\mathrm{MPa}$
T1-Relaxometry	$\overline{\mathrm{T}}_1 = 5.720\,\mathrm{ms}$	$\sigma(\mathrm{T}_1) = 0.03\,\mathrm{ms}$
Ramsey	$\overline{\mathrm{T}}_2^* = 1.67\,\mu\mathrm{s}$	$\sigma(\mathrm{T}_2^*) = 0.04\,\mu\mathrm{s}$
Hahn-echo	$\overline{\mathrm{T}}_2 = 11.9\,\mu\mathrm{s}$	$\sigma(\mathrm{T}_2) = 0.1\,\mu\mathrm{s}$

to boil off both the nitric and nerchlorate acids. Sulfuric acid is still liquid at this temperature, and remains in the flask as the final product (as well as any etched contaminants). The fumes from the boiling process are passed through a condenser unit into a flask with DI water in order to capture the boiled acids for disposal. The post-condensed gas is then passed through a gas wash bottle in order to remove any trace remaining acid vapors. During setup, care must be taken that the total DI water used in the gas wash bottle and condenser flask do not exceed the total volume of the condenser flask, as water from the former can be ingested into the latter when the heat is turned off.

X-ray photoelectron spectroscopy (XPS) is conducted using a Kratos Axis Ultra with monochromatic Al K_α 1486.7eV excitation source operating at 15kV and 10mA. XPS collected before and after the etch process confirms the change in surface chemistry, including a reduction in surface O1s signal, and the effective elimination of Si, Na and Cl. Also notably, the C1s energy becomes sharper after treatment, suggesting a homogenization of the surface carbon bond environment by removal of graphitic carbon, see Fig. S6.

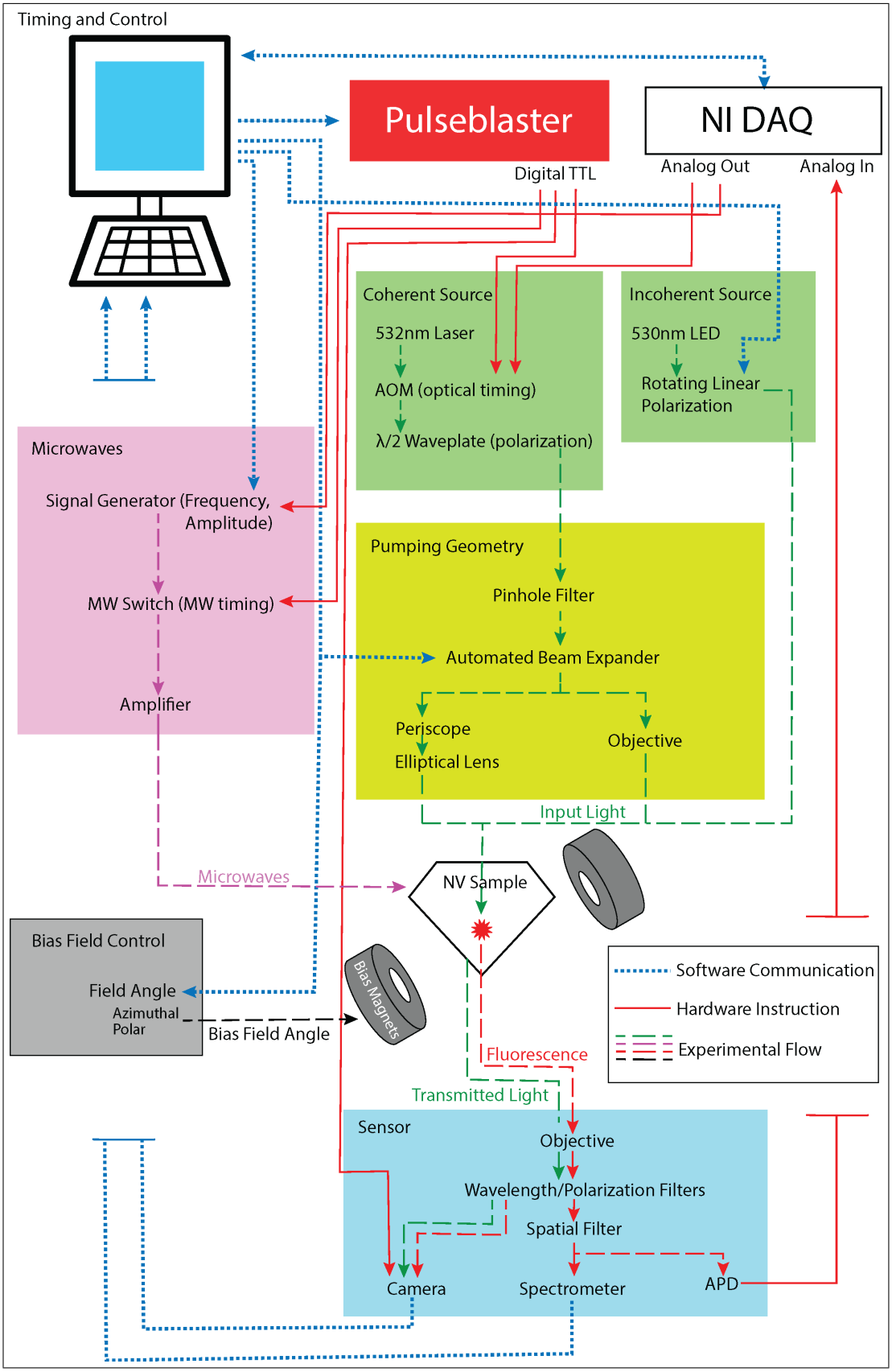


FIG. S1. Schematic of all-in-one QDM components and their interrelationships.

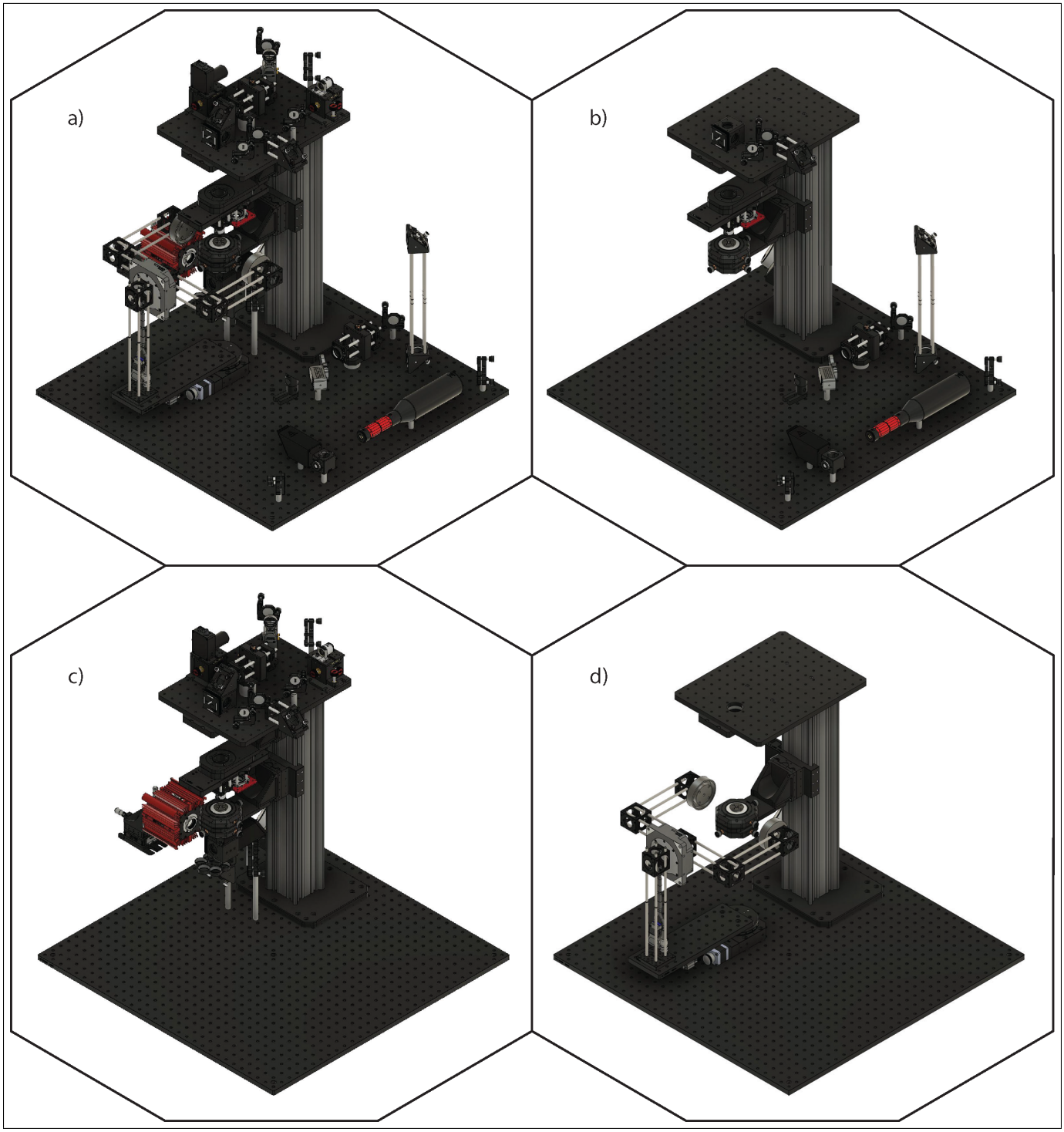


FIG. S2. CAD setup of all-in-one QDM subsystems. a) Optical-breadboard components, with the exception of acousto-optic modulator (AOM). Electronics and non-LGR MW components (including antenna coupled to LGR) are omitted. b) Components involved in shaping and polarization of input laser signal, including beam splitter for linear polarization control, motorized beam expander, optional pinhole for TEM00 beam mode shaping, periscope option for low-angle excitation, LED module and rotator on switchable stage, and top objective for transmission birefringence measurement option. c) NV PL and LED transmission collection optics, including long-pass filter, optional pinhole for confocal image, and flipper mirror for PL collection either by photodiode or fiber-coupled spectrometer. d) Bias magnet system, including two motors for control over field angle.

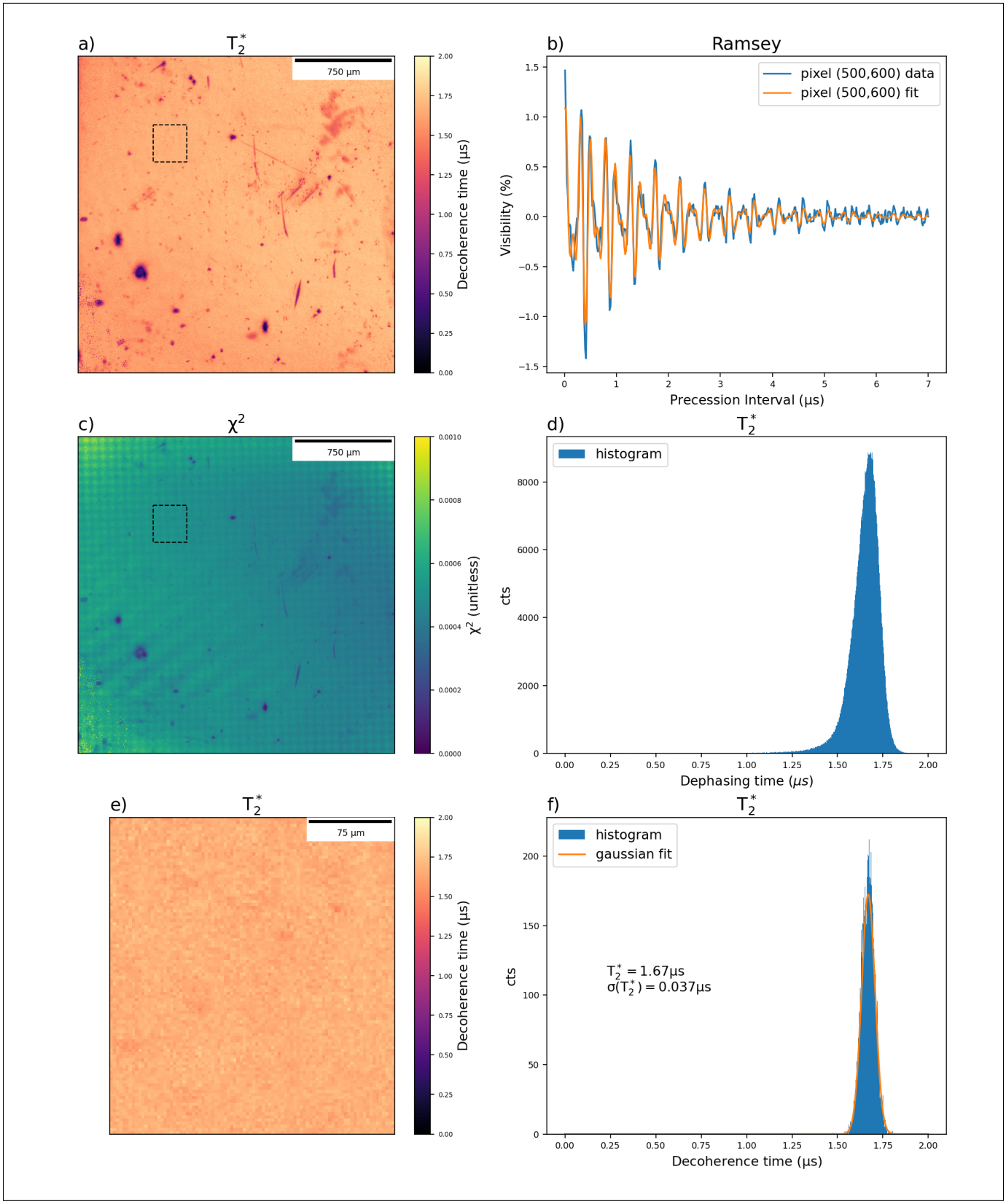


FIG. S3. Evaluation methods for Ramsey fitting dataset. a) Map of NV diamond sample T_2^* values, box corresponds to homogeneous (low strain) sub-region selected for further analysis. b) Example single-pixel Ramsey data and corresponding fit. Fit's decay envelope corresponds to pixel value used in T_2^* map. c) χ^2 map of associated fits in same field-of-view as T_2^* map in a). d) Histogram of T_2^* values from a), broadened asymmetrically by regions of strain and surface contaminants. e) Map of T_2^* values for boxed sub-region in a). f) Histogram of T_2^* values from e), and corresponding Gaussian fit giving median $T_2^* = 1.67\mu s$ and standard deviation $\sigma = 0.037\mu s$, corresponding to a confidence interval of about 2.2%. Similar techniques are used to evaluate convergence in other imaged modalities.

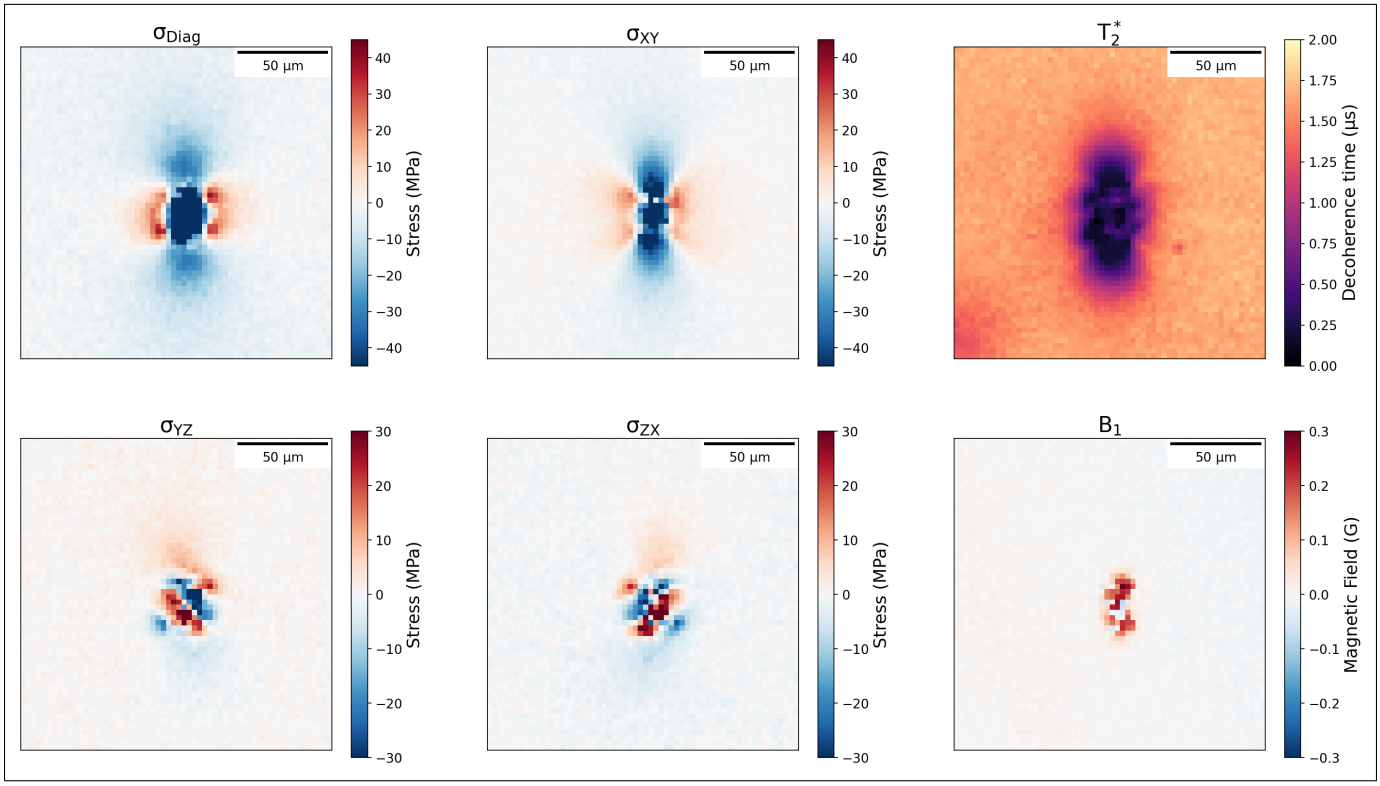


FIG. S4. Maps of key strain observables near a defect bundle. CW-ODMR detected strain tensor components show highly-resolved features particular to the bundle symmetry, while T_2^* shows significant degradation co-located with diagonal strain components. B_1 as measured by CW-ODMR along a particular NV axis shows spurious magnetic features, demonstrating a particular example of how a well known defect process can introduce strain gradients that negatively affect sensing.

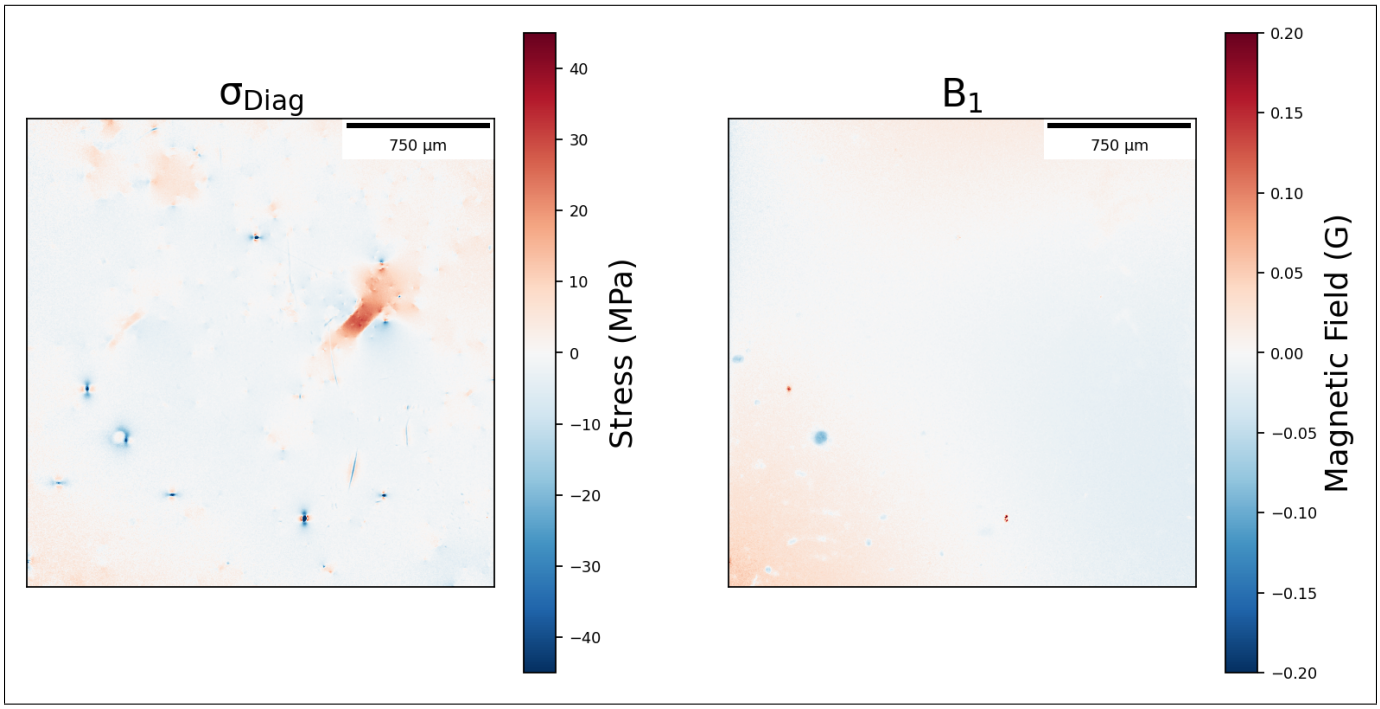


FIG. S5. A comparison between maps of CW-ODMR detected strain and CW-ODMR detected magnetic field for a single NV direction across the sample field of view presented in the main text. Several co-registered defects are visible in both modalities, indicating specific inhomogenous strain regions where magnetic sensitivity is compromised.

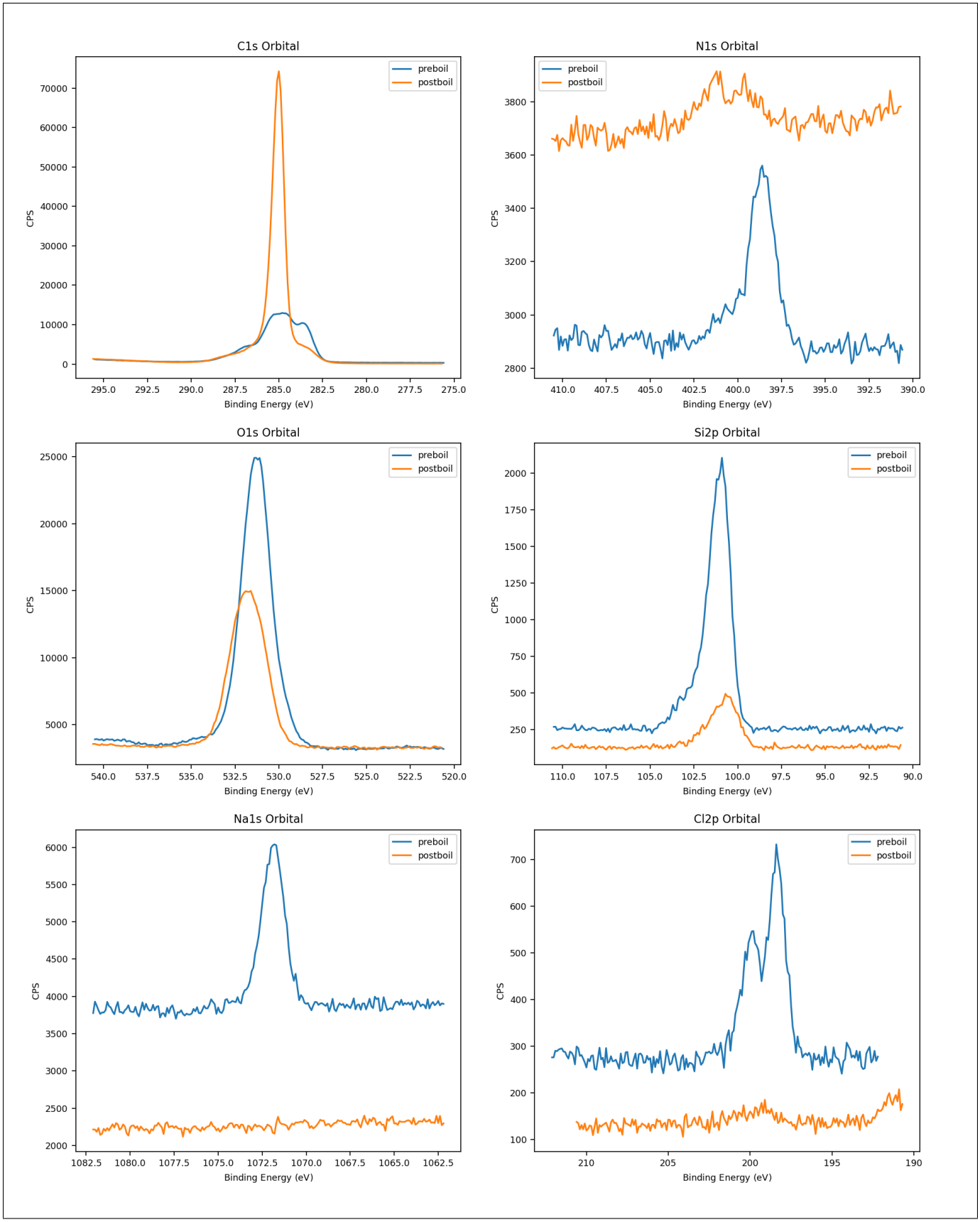


FIG. S6. XPS results before and after perchlorate etch for several atomic species. Silicon and several common species decreased with etching, and Carbon 1s orbitals are significantly homogenized. Surface N also appears to be strongly suppressed.